ЖЭТФ, 2016, том 149, вып. 5, стр. 1030–1042

OPTICAL EVIDENCE OF QUANTUM ROTOR ORBITAL EXCITATIONS IN ORTHORHOMBIC MANGANITES

N. N. Kovaleva [a,b,c*], ***K. I. Kugel*** [b,d], ***Z. Potůček*** [e], ***O. E. Kusmartseva*** [b], ***N. S. Goryachev*** [f], ***Z. Bryknar*** [e], ***E. I. Demikhov*** [a], ***V. A. Trepakov*** [c,g], ***A. Dejneka*** [c], ***F. V. Kusmartsev*** [b], ***A. M. Stoneham*** [h]

[a] *Lebedev Physical Institute, Russian Academy of Sciences 119991, Moscow, Russia*

[b] *Department of Physics, Loughborough University LE11 3TU Loughborough, United Kingdom*

[c] *Institute of Physics, Academy of Sciences of the Czech Republic 18221, Prague, Czech Republic*

[d] *Institute for Theoretical and Applied Electrodynamics, Russian Academy of Sciences 125412, Moscow, Russia*

[e] *Czech Technical University, 12000, Prague, Czech Republic*

[f] *Institute of Problems in Chemical Physics, Russian Academy of Sciences 142432, Chernogolovka, Moscow Region, Russia*

[g] *Ioffe Physical-Technical Institute, Russian Academy of Sciences 194021, Saint-Petersburg, Russia*

[h] *London Centre for Nanotechnology, University College London WC1H OAH London, United Kingdom*

Received November 11, 2015

In magnetic compounds with Jahn–Teller (JT) ions (such as Mn^{3+} or Cu^{2+}), the ordering of the electron or hole orbitals is associated with cooperative lattice distortions. There the role of JT effect, although widely recognized, is still elusive in the ground state properties. Here we discovered that, in these materials, there exist excitations whose energy spectrum is described in terms of the total angular momentum eigenstates and is quantized as in quantum rotors found in JT centers. We observed features originating from these excitations in the optical spectra of a model compound $LaMnO_3$ using ellipsometry technique. They appear clearly as narrow sidebands accompanying the electron transition between the JT split orbitals on neighboring Mn^{3+} ions, displaying anomalous temperature behavior around the Néel temperature $T_N \approx 140$ K. We present these results together with new experimental data on photoluminescence found in $LaMnO_3$, which lend additional support to the ellipsometry implying the electronic-vibrational origin of the quantum rotor orbital excitations. We note that the discovered orbital excitations of quantum rotors may play an important role in many unusual properties observed in these materials upon doping, such as high-temperature superconductivity and colossal magnetoresistance.

DOI: 10.7868/S0044451016050126

1. INTRODUCTION

Orbital ordering phenomena in correlated electron systems with electron–phonon interaction remains an actively developing field of research despite many years of scientific effort. In magnetic compounds with Jahn–Teller ions (such as Mn^{3+} or Cu^{2+}), the ordering of the e_g electron or hole orbitals not only leads to cooperative lattice distortions but also determines their magnetic properties. In addition to a more traditional electron–lattice Jahn–Teller (JT) mechanism of orbital

* E-mail: nkovaleva@sci.lebedev.ru

ordering [1–6], a purely electronic superexchange (SE) mechanism can also lead to the formation of the orbital and magnetic ordering [7–9].

Orthorhombic rare-earth (RE) manganites $REMnO_3$ (RE = La, Pr, Nd, Sm, Eu, Gd, Tb, Dy) are regarded to be model compounds in orbital physics: these systems are perovskites with the Mn^{3+} ions having the $t_{2g}^3 e_g^1$ electronic configuration. Their high-temperature phase is nearly cubic, and at the temperature T_{oo}, they undergo a transition into the orthorhombic orbitally ordered *Pbnm* structure with an antiferrodistorsive ordering of MnO_6 octahedra (see Fig. 1*a,b*). Recent *ab initio* studies demonstrate that the SE interaction alone cannot initiate the transition at T_{oo} [10]. Another argument supporting the importance of the JT mechanism comes from the fact that the SE favors the occupation of the e_g orbital with the orbital angle $\theta = 90°$. In fact, the orbital angle determined from the neutron scattering for $LaMnO_3$ is $\theta \sim 108°$ [11], and this difference further increases in the manganites with smaller ionic radii to $\theta \sim 114°$ for $TbMnO_3$ [12]. For comparison, the orbital angle of an isolated JT MnO_6 complex is $\theta = 120°$. Moreover, in our recent study of polarized Raman scattering in the untwinned $LaMnO_3$ crystal, it is shown that the multi-order phonon density of states observed there up to the fourth order is the sidebands on the low-energy mode at 24 cm^{-1} [13]. This specifies that the low-energy mode at 24 cm^{-1} stems from the tunneling transition between the potential energy minima arising near the JT Mn^{3+} ion due to lattice anharmonicity. These indications suggest that the nature of the ground state in orthorhombic manganites is more pertinent to the JT ground state.

In agreement with the JT theorem [1], an octahedral MnO_6 complex placed in cubic symmetry surroundings suffers a JT distortion to a state of reduced symmetry and lower energy. Here, the ground state is stabilized by splitting the doubly degenerate electronic levels of an Mn^{3+} ion by a vibronic interaction between the $d_{3z^2-r^2}$ and $d_{x^2-y^2}$ symmetry orbitals and the Q_2 and Q_3 normal modes. If only the linear vibronic coupling terms are taken into account, the ground-state energy of the MnO_6 complex has an infinite degeneracy, associated with the symmetry of the distortions invariant under rotations in the (Q_2, Q_3) normal coordinates. This means that the ground state is not uniquely defined, but occurs at any point of the circle with the radius $\rho_0 \equiv \sqrt{Q_{20}^2 + Q_{30}^2}$ along the trough at the bottom of the adiabatic potential energy surface called the "Mexican hat" (see Fig. 1*c*). There are no barriers to hinder rotations in the (Q_2, Q_3) plane, and the oscillations in the configuration of the MnO_6 octahedron without a change in energy lead to the dynamic JT effect.

However, the infinite degeneracy of the ground state may be removed if one takes third-order (anharmonicity) terms of the normal coordinates Q_2 and Q_3 into account in the expansion of a potential energy, which results in the appearance of three discrete minima in the trough of the "Mexican hat" [2]. And at a sufficiently low temperature, the system may become localized in one of them associated with the tetragonal *static* lattice distortion. The minima on the low energy surface of the deformed "Mexican hat" are separated by potential barriers. Their influence on the stability of the ground state was considered by O'Brien [14], who first investigated the quantum energy levels in this system. Their eigenvalues associated with the $\mathbf{A}_1$, $\mathbf{A}_2$, and $\mathbf{E}$ irreducible representations of the C_{3v} symmetry group were estimated. The results are presented in the diagram as a function of the potential barrier height β (see Fig. 1*d*). There is also the energy splitting parameter α used in the quantization of discrete energy levels [14]. As follows from the diagram, the $\mathbf{E}$ energy level is associated with the ground state with the quantum number of the angular momentum around the potential trough $j = \pm 1/2$. In the dynamic limit ($\beta = 0$), energies of the rotor excitations generate a sequence determined by the quadratic dependence on values of the angular momentum j, $\varepsilon = \alpha j^2$. These levels are associated with the dynamic limit of rotor excitations. Their energy levels shift with increasing the barrier height β in a static limit. Thus, for the two extreme limits of the barrier height β, we can have a dynamic fast-rotation limit for $\beta = 0$ and a static slow-rotation limit for $\beta \to \infty$.

The quantum rotor excitations, considered by O'Brien [14], are referred to the lower-energy "Mexican hat" surface and exist near the ground state of JT ions. One can probe these excitations by using the Raman scattering technique. In our recent Raman study of $LaMnO_3$, we had observed some of these excitations, which are obscured by the phonon density-of-states feature, and described them as excitations of unknown origin [13]. However, quantum rotor excitations, similar to those considered by O'Brien [14], can also be referred to the upper-energy "Mexican hat" surface and exist near the excited state of JT ions. Here, we applied spectroscopic ellipsometry to study in detail the low-energy dielectric function spectra of a model JT compound $LaMnO_3$ above the excitation edge in the temperature range 20–300 K. The spectra are dominated by the optical band at 2 eV, which is associated with the electron transition between the JT split

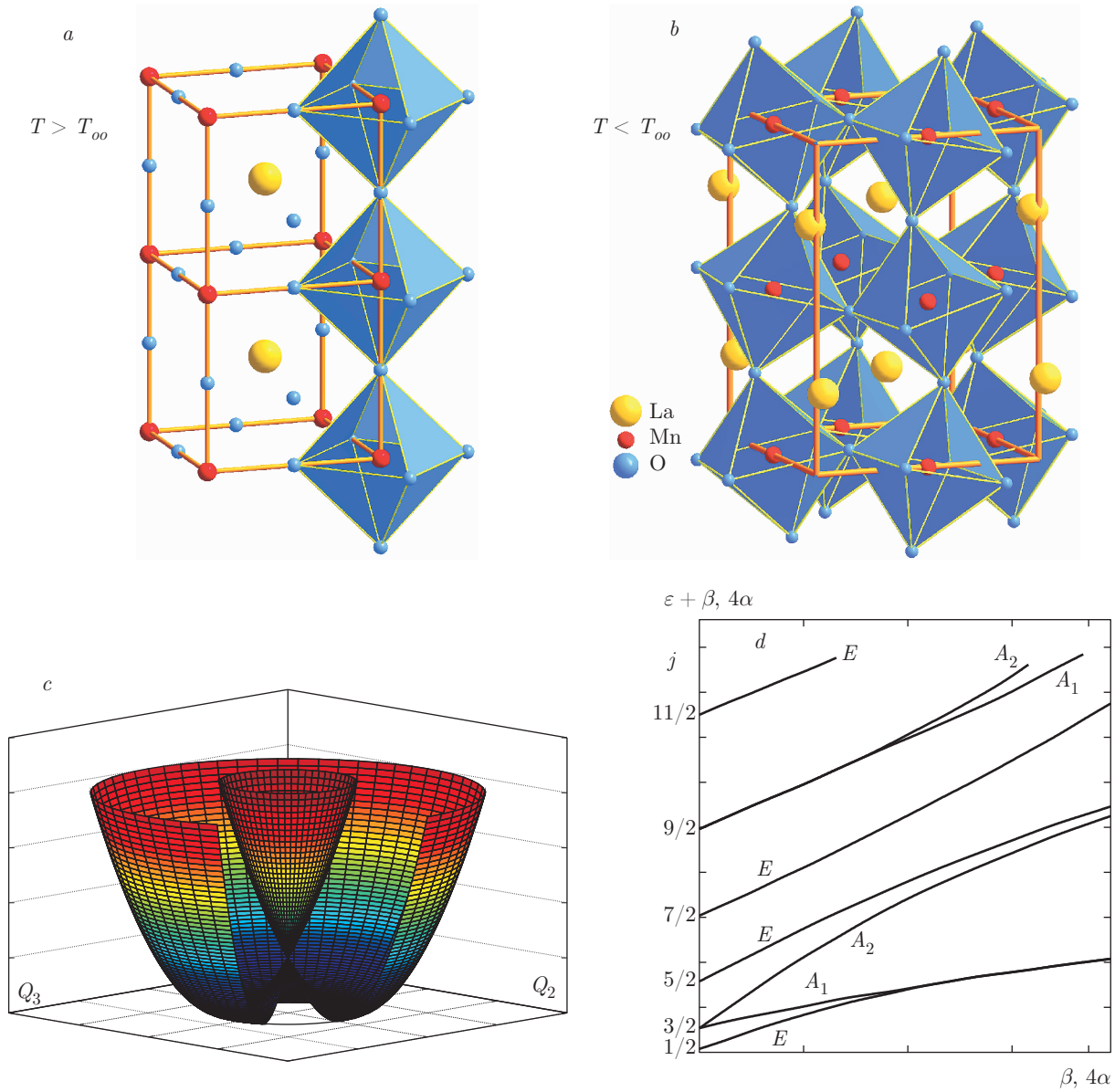

Fig. 1. (Color online) (a) Structure of the high-temperature pseudo-cubic perovskite phase of rare-earth manganites $REMnO_3$. (b) Structure of the orthorhombic $Pbnm$ phase of $REMnO_3$ below the orbital ordering temperature T_{oo}. (c) Double-valued "Mexican hat" potential energy surface of an octahedral MnO_6 complex for linear vibronic coupling (dynamic limit) in the normal coordinates Q_2 and Q_3. The "Mexican hat" deformed by third-order (anharmonicity) terms has three discrete minima at the bottom of the trough, separated by anharmonicity barriers (not shown). (d) Energies in the "Mexican hat" as functions of the barrier parameter β. Values of the angular momentum $j = 1/2, 3/2, 5/2, \ldots$ are given in the dynamic limit. Results after O'Brien [14]

orbitals on neighboring Mn^{3+} ions [15, 16]. We discovered a series of narrower satellite excitations above this transition in the 2.2–2.9 eV spectral range. Similar spectral features are observed in optical spectra of many orthorhombic RE manganites $REMnO_3$ [17, 18]. The higher-energy excitations exhibit an anomalous temperature dependence around the Néel temperature $T_N \approx 140$ K. As a result, they appear as prominent optical bands in the **a**-axis room-temperature (**c**-axis low-temperature) spectra, or may become almost washed out in the **a**-axis low-temperature (**c**-axis room-temperature) spectra. Our analysis showed that the discovered excitations are closely related to quantum rotor excitations in the "Mexican hat" profile of the

Mn^{3+} ions. Here, we also introduce new data on photoluminescence properties of $LaMnO_3$. The observed emission occurs from the same resonant energy levels in the 2.2–2.9 eV spectral range, which is indicative of their electron-vibrational (vibronic) origin. The quantum rotor excitations depend on values of the angular momentum j, $\varepsilon = \alpha j^2$, and can be regarded as orbital excitations. We note that the discovered orbital excitations of quantum rotors may play an important role in many unusual properties observed in magnetic compounds with JT ions (Mn^{3+} or Cu^{2+}) upon doping, such as high-temperature superconductivity and colossal magnetoresistance.

2. EXPERIMENTAL APPROACH AND RESULTS

2.1. Crystal growth

$LaMnO_3$ single crystals were grown by the crucible-free floating zone method using an image furnace equipped with an arc lamp [19, 20]. The as-grown $LaMnO_3$ single crystals are single phased, but exhibit heavily twinned domain patterns in the orthorhombic *Pbnm* structure (where the **c** axis is a long axis of the unit cell) at temperatures below the orbital ordering temperature $T_{oo} \approx 780$ K. We were able to remove the twins from an essential part (85 %) of the sample volume using the procedure described in detail in our previous study [16]. We determined an antiferromagnetic transition at the Néel temperature $T_N \approx 139.6$ K, which is characteristic of a nominally oxygen-stoichiometric $LaMnO_3$ crystal [21].

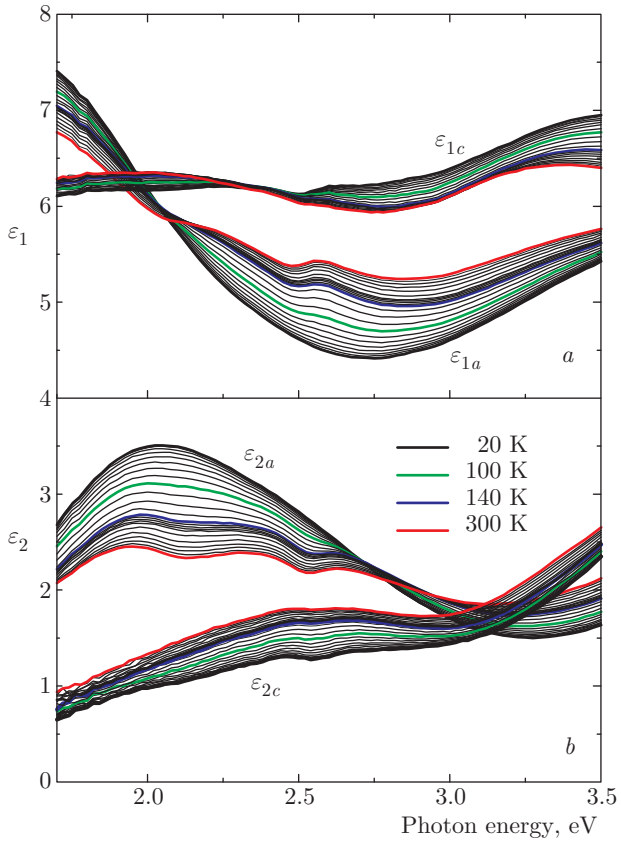

Fig. 2. (Color online) Temperature variation of the **a**- and **c**-axis (*a*) real $\varepsilon_1(\nu)$ and (*b*) imaginary $\varepsilon_2(\nu)$ parts of the low-energy complex dielectric function spectra of the untwinned $LaMnO_3$ crystal. The representative spectra at the temperatures around $T_N \approx 140$ K are indicated. The temperature evolution is shown in successive temperature intervals of 10 K between 20 and 160 K and of 25 K between 175 and 300 K

2.2. Low-energy optical dielectric function spectra of the untwinned $LaMnO_3$ crystal

By using spectroscopic ellipsometry technique, we investigated anisotropic **a**- and **c**-axis dielectric function spectra of the nominally stoichiometric untwinned $LaMnO_3$ crystal at different temperatures from 10 to 300 K. The complex dielectric function spectra of $LaMnO_3$ were investigated in the photon energy range 0.75–6.0 eV using a home-built ellipsometer of a rotating-analyzer type [22] with the angle of incidence 70.0° at the Max-Planck-Institut für Festkörperforschung, Germany. The sample was mounted on a cold finger of a helium flow UHV cryostat, where the temperature varied between 10 and 300 K. To avoid contamination of the sample surface with ice, we evacuated the cryostat to a base pressure of about $5 \cdot 10^{-9}$ Torr at room temperature. The spectroscopic ellipsometry approach offers significant advantages over conventional reflection methods because (i) it is self-normalizing and does not require reference measurements and (ii) the full complex dielectric function spectra $\varepsilon(\nu) = \varepsilon_1(\nu) + i\varepsilon_2(\nu)$ represented by real $\varepsilon_1(\nu)$ and imaginary $\varepsilon_2(\nu)$ parts can be obtained directly without the Kramers–Kronig transformation.

Figure 2*a,b* shows the temperature dependence of the **a**- and **c**-axis real $\varepsilon_1(\nu)$ and imaginary $\varepsilon_2(\nu)$ parts of the dielectric function spectra of the untwinned $LaMnO_3$ crystal above the absorption edge. We can see that the **c**-axis dielectric function spectra are strongly suppressed compared to the **a**-axis spectra due to the crystalline anisotropy. The low-energy dielectric function spectra are dominated by a broad optical band peaking at around 2 eV, identifiable in Fig. 2*a,b* by antiresonance and resonance features, obeying the Kra-

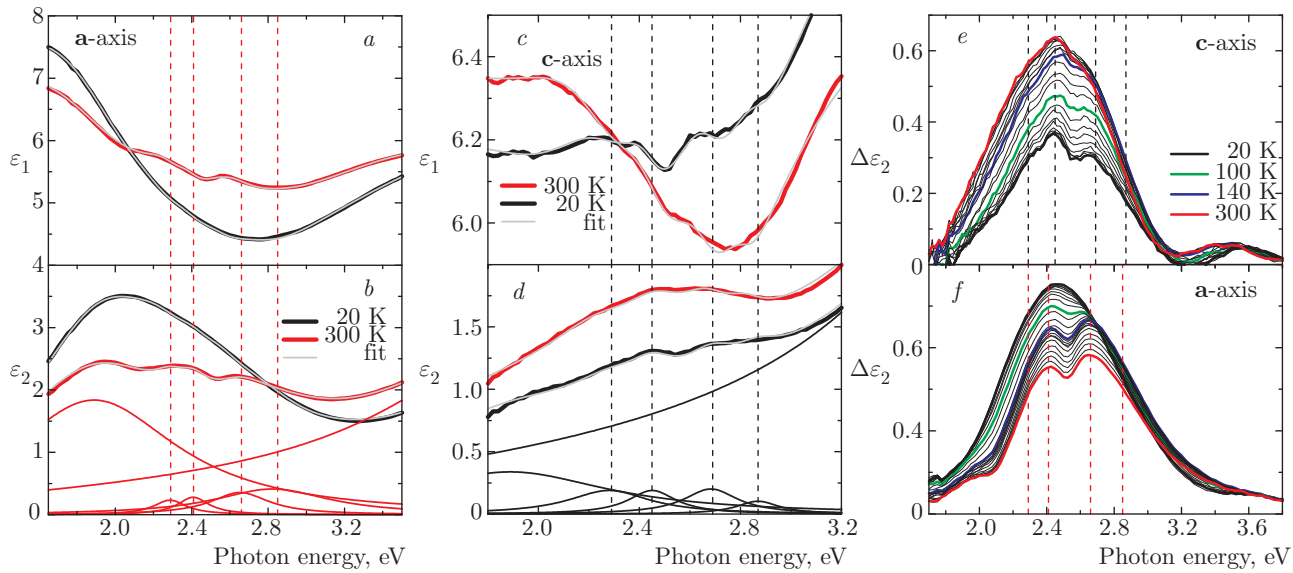

Fig. 3. (Color online) (*a*,*c*) Real $\varepsilon_1(\nu)$ and (*b*,*d*) imaginary $\varepsilon_2(\nu)$ parts of the **a**- and **c**-axis dielectric function spectra $\varepsilon(\nu)$ at 20 K and at 300 K, fitted by the Lorentzian oscillators according to the classical dispersion analysis procedure. The five Lorentzian bands determined from the fit of the $\varepsilon(\nu)$ spectra in the **a** axis at 300 K and in the **c**-axis at 20 K are drawn; the corresponding resonant energies of the four higher-energy satellites are marked by the dashed lines. (*e*,*f*) The cumulative temperature dependence of the four marked higher-energy excitations in the **a**- and **c**-axis spectra, resulting from the dispersion analysis

mers–Kronig relations, which appear at this energy in $\varepsilon_1(\nu)$ and $\varepsilon_2(\nu)$, respectively. Superimposed are a number of smaller higher-energy spectral features, which look more pronounced in the **a**-axis spectra and less pronounced in the **c**-axis spectra. As follows from Fig. 2*a*,*b*, the anisotropy of the low-energy complex dielectric function spectra increases with decreasing temperature, and is accompanied by pronounced temperature dependence of the constituent optical bands. As a result, the higher-energy bands appear as sharp features in the **a**-axis room-temperature spectra and in the **c**-axis low-temperature spectra, or may become almost washed out in the **c**-axis room-temperature spectra and in the **a**-axis low-temperature spectra (see also Fig. 3*a*–*d*). The **c**-axis low-temperature $\varepsilon(\nu)$ spectra indicate that the higher-energy multi-band structure consists of four bands, recognizable by the Kramers–Kronig consistent resonance and antiresonance features marked by the dashed lines in Fig. 3*c*,*d*.

To separate contributions from the optical bands, which show onset above 3 eV, and to extract the temperature-dependent contribution of the constituent low-energy optical bands, we performed a classical dispersion analysis of the temperature-dependent complex dielectric function in the studied spectral range. Using the dielectric function of the form

$$\varepsilon(\omega) = \epsilon_\infty + \sum_j \frac{S_j \nu_j^2}{\nu_j^2 - \nu^2 - i\nu\gamma_j},$$

where ν_j, γ_j, and S_j are the peak energy, the full width at half maximum (FWHM), and the dimensionless oscillator strength of the jth oscillator, and ϵ_∞ is the core contribution to the dielectric function [23], we fitted a minimum set of Lorentz oscillators simultaneously to $\varepsilon_1(\nu)$ and $\varepsilon_2(\nu)$.

Our fit accurately reproduces the temperature-dependent anisotropic complex dielectric function spectra in the studied temperature range, as illustrated by Fig. 3*a*–*d*. Figure 3*a*–*d* shows the real $\varepsilon_1(\nu)$ and imaginary $\varepsilon_2(\nu)$ parts of the **a**- and **c**-axis low-energy dielectric function spectra $\varepsilon(\nu)$ at 20 K and at 300 K, fitted by the Lorentzian oscillators according to the described procedure of the classical dispersion analysis. It indicates that the low-energy multi-band structure is represented by a pronounced optical band at about 2 eV and four weaker and narrower higher-energy bands. According to the results illustrated by Fig. 3*a*–*d*, the higher-energy bands appear at nearly the same resonant energies (within the pretended accuracy) in the room-temperature **a**-axis spectra at 2.29 ± 0.02 eV, 2.41 ± 0.02 eV, 2.66 ± 0.02 eV, and 2.84 ± 0.02 eV, and in the low-temperature **c**-axis spectra at 2.29 ± 0.02 eV,

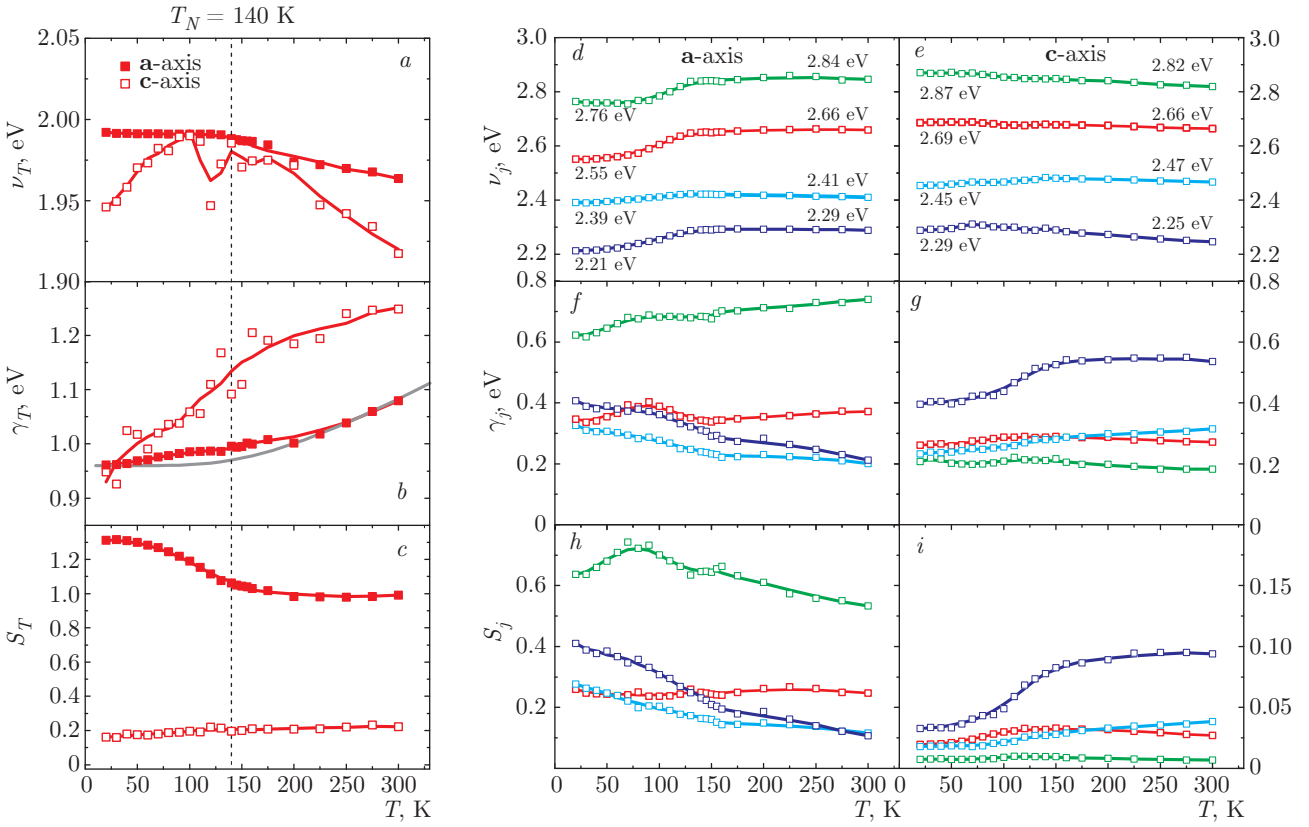

Fig. 4. (Color online) Temperature dependence of (*a*) the peak energy ν_T, (*b*) the full width at half maximum (FWHM) γ_T, and (*c*) the oscillator strength S_T of the pronounced low-energy band at 2 eV. Temperature dependence of (*d*,*e*) the peak energy ν_j, (*f*,*g*) the FWHM γ_j, and (*h*,*i*) the oscillator strength S_j of the four higher-energy satellites in the **a**- and **c**-axis, resulting from the dispersion analysis

2.45 ± 0.02 eV, 2.69 ± 0.02, and 2.87 ± 0.02 eV. Figure 4*a*–*i* summarizes the detailed T-dependence of the peak energy ν_T, the FWHM γ_T, and the oscillator strengths S_T of the strongly pronounced optical band at about 2 eV, as well as those of the four higher-energy bands, the ν_j, the FWHMs γ_j, and the oscillator strengths S_j, resulting from the dispersion analysis of the two independent sets of temperature-dependent **a**- and **c**-axis complex dielectric function spectra. The fit of the **a**-axis data was stable, and the deduced parameters of ν_T, γ_T, and S_T were determined within the estimated accuracy in the whole studied temperature range. However, we note that due to deficiency of the data below 1.7 eV, the parameters ν_T, γ_T, and S_T deduced from the **c**-axis data are less accurate, especially at low temperatures due to strong signal suppression, where trends inferred from the fit should be taken with care (and are not under discussion here).

We first analyze the temperature dependence of the parameters ν_T and γ_T obtained for the strongly pronounced optical band at about 2 eV (see Fig. 4*a*,*b*); the temperature behavior of S_T (shown in Fig. 4*c*) is discussed later. We can see from Fig. 4*a* that below T_N, the peak position in the **a** axis remains practically constant at 1.98 eV. The peak position ν_T exhibits a noticeable red shift above the T_N at elevated temperatures in the **a**- and **c**-axis spectra due to lattice anharmonicity. At the same time, the band FWHM γ_T displays appreciable broadening (Fig. 4*b*). In systems with strong electron–phonon interaction, the optical band shape is determined according to the Franck–Condon principle. When the adiabatic potentials of the ground and excited states are strongly displaced, multiphonon transitions occur with high probability and thus a broad intense band is observed. The zero-phonon line in such cases may have a small intensity or may be completely absent. This particular case seems to be relevant to the optical band at about 2 eV, which is strongly pronounced in the **a**-axis $\varepsilon_2(\nu)$ spectra and has a FWHM of about 1 eV at low

temperatures. In the conventional Huang–Rhys theory, the bandwidth has the root-mean-square value $\hbar\omega_0\sqrt{S} \equiv \hbar\omega_0\sqrt{S_0\mathrm{coth}(\hbar\omega_0/k_BT)}$, and the low-temperature limit $\hbar\omega_0\sqrt{S_0}$, where S_0 is the Huang–Rhys factor and $\hbar\omega_0$ is the effective phonon frequency. Here, the temperature dependence of the FWHM is determined by the temperature dependence of electron–lattice interaction via $S \equiv S_0\mathrm{coth}(\hbar\omega_0/k_BT)$ [24]. Taking the low-temperature limit for the FWHM of the 2 eV optical band in the **a**-axis from our data, $\hbar\omega_0^a\sqrt{S_0^a} \approx 0.96$ eV, we were able to accurately fit the FWHM temperature dependence in the 200–300 K temperature range (we note that here, well above the $T_N \approx 140$ K, the bandwidth should not be noticeably affected by magnetic interactions) by the formula $\hbar\omega_0^a\sqrt{S_0^a\mathrm{coth}(\hbar\omega_0^a/k_BT)}$ and estimate the effective phonon frequency $\hbar\omega_0^a \approx 27.5$ meV (see Fig. 4*b*). The determined effective phonon frequency $\hbar\omega_0$ is associated with the longitudinal optical phonon mode in $LaMnO_3$ [25, 26]. In the corresponding transverse optical phonon mode, oxygen vibrations in the MnO_2 plane modulate the total dipole moment along the **a**-axis direction [25]. From Fig. 4*b*, we can see that the **a**-axis FWHM exhibits a deviation from the law $\hbar\omega_0^a\sqrt{S_0^a\mathrm{coth}(\hbar\omega_0^a/k_BT)}$, which sets on below 200 K, indicating additional physics involved around the Néel temperature $T_N \approx 140$ K.

Next, we analyze the temperature dependence of the parameters ν_j and γ_j deduced for the four **a**- and **c**-axis higher-energy bands, arising above the pronounced 2 eV optical band in the 2.2–2.9 eV spectral range (see Fig. 4*d–g*); the temperature behavior of the S_j (shown in Fig. 4*h,i*) is discussed later. We start with the analysis of the **a**-axis temperature behavior of the higher-energy bands, which appear at room temperature at 2.29 ± 0.02 eV, 2.41 ± 0.02 eV, and 2.66 ± 0.02 eV. First of all, we note that the bands are relatively narrow, with their FWHM in the range 0.2–0.4 eV, which is indicative of their peculiar origin. We found that the peak positions ν_j are almost independent of temperature above T_N. Moreover, the peaks ν_j at about 2.29 and 2.66 eV showed a sharp shift down, by about 80 and 110 meV, respectively, to lower energies below the Néel temperature T_N. At the same time, the peak at about 2.41 eV remained practically unchanged in the investigated temperature range. In addition, the FWHMs of the two first **a**-axis higher-energy bands, represented by single Lorentz oscillators, exhibited an anomalous temperature dependence. From Fig. 4*f*, it can be seen that their FWHMs decrease from about 0.4 to 0.2 eV as the temperature increases from low values to $T_N \approx 140$ K. The disclosed temperature behavior of the **a**-axis higher-energy bands is certainly beyond the lattice anharmonicity law, which suggests a red shift of peak energies and band broadening at elevated temperatures.

In the **c**-axis, the corresponding higher-energy bands appear at low temperature at 2.29 ± 0.02 eV, 2.45 ± 0.02 eV, and 2.69 ± 0.02 eV. Here, the band peak energies ν_j and their FWHMs γ_j show opposite trends with increasing temperature. Namely, the peaks ν_j at 2.29 and 2.69 eV show a noticeable shift down, by about 40 and 30 meV, respectively, to lower energies with increasing the temperature from 20 to 300 K. Similarly to the **a**-axis behavior, the peak position at about 2.45 eV remains practically unaffected in the investigated temperature range (see Fig. 4*e*). We found that the FWHM of the 2.29 eV band exhibited a sharp increase from about 0.4 to 0.47 eV with changing the temperature from low values to T_N (see Fig. 4*g*). However, the FWHMs of other bands at 2.45 and 2.68 eV were much more weakly influenced in the studied temperature range.

And finally, we discuss temperature behavior of the 2.8 eV optical band, which appears in the room-temperature **a**-axis spectra at 2.84 ± 0.02 eV and in the low-temperature **c**-axis spectra at 2.87 ± 0.2 eV. The band is highly anisotropic. It looks pronounced in the **a**-axis $\varepsilon_2(\nu)$ spectra, but is strongly suppressed in the **c**-axis $\varepsilon_2(\nu)$ spectra, as can be seen from Fig. 3*b,d*. At the same time, the band is relatively wide in the **a**-axis spectra, and its FWHM γ_j displays an appreciable broadening from about 0.6 to 0.8 eV with increasing temperature in the studied temperature range (see Fig. 4*f*). The bandwidth broadening at elevated temperatures in the **a**-axis can be associated with ordinary lattice anharmonicity effects. On the other hand, the FWHM in the **c**-axis is much less, of about 0.2 eV, and only weakly depends on temperature (see Fig. 4*g*). The peak in the **a**-axis ν_j at about 2.84 eV shows a sharp shift down by about 80 meV to lower energies below T_N (see Fig. 4*d*). And the peak in the **c**-axis ν_j at about 2.87 eV shows a shift down by about 50 meV to lower energies with increasing the temperature from low to room temperature (see Fig. 4*e*). Summarizing, we note that the temperature trends exhibited by 2.8 eV band are largely similar to those shown in Fig. 4*d,e* for the other higher-energy bands.

Based on the results of our dispersion analysis, we extracted the total temperature-dependent contribution of the four higher-energy bands to the **a**- and **c**-axis $\varepsilon_2(\nu)$ dielectric function spectra, separated from the dominant low-energy optical band at about 2 eV and from the optical transitions arising above 3 eV

(see Fig. 3*e,f*). We can see that the extracted optical response exhibits prominent temperature dependence around the Néel temperature in the **a**- and **c**-axis spectra. As a result of the disclosed temperature behavior of the constituent **a**- (**c**-) axis higher-energy bands, the bands appear as sharp features at room temperature (low temperature), or may become almost washed out at low temperature (room temperature). This behavior is quite impressive and can already be seen in the spectra of the temperature-dependent dielectric function $\varepsilon_2(\nu)$ in Fig. 2*b*.

2.3. Photoluminescence properties of a nominally stoichiometric $LaMnO_3$ crystal

For photoluminescence (PL) measurements, the $LaMnO_3$ single crystal was fixed to a copper holder of a closed-cycle helium refrigerator. The PL emission was measured in right-angle geometry in the temperature range 10–350 K, using a setup equipped with a SPM 2 grating monochromator (Carl Zeiss). The PL was excited with light from a high-pressure Xe lamp filtered through a double-grating Jobin-Yvon DH 10UV monochromator. The emission was detected in the spectral range 350 nm (3.54 eV)–870 nm (1.46 eV) with a cooled RCA 31034 photomultiplier (with a GaAs photocathode) operating in the photon-counting mode. The emission spectra were taken with a spectral resolution of 6 nm and corrected for the apparatus spectral dependence. The PL excitation spectra were referred to a constant flux of excitation light over the whole studied spectral range.

Figure 5*a* shows the PL emission spectra measured on the same $LaMnO_3$ single crystal under excitation by light with a photon energy of 4.6 eV at different temperatures from 10 to 300 K. The PL emission was observed in a broad spectral range (of about 0.7 eV), peaking near 2.5 eV at 10 K. The peak showed a shift to lower energies with increasing temperature, and its relative intensity exhibited a sharp decrease below about 200 K. We note that no drastic changes of the relative intensity were observed across T_N. Figure 5*b* shows the PL excitation spectra registered for the fixed PL emission energies of 2.3 and 2.5 eV at $T \approx 10$ K. In Fig. 5*b*, the PL excitation spectra are superimposed with the **a**- and **c**-axis dielectric function spectra, $\varepsilon_2^{\mathbf{a},\mathbf{c}}(\nu)$, measured on the same untwinned $LaMnO_3$ single crystal at $T \approx 10$ K. The $\varepsilon_2^{\mathbf{a},\mathbf{c}}(\nu)$ spectra are consistent with the data presented in Fig. 2*b*. The PL excitation spectra show a pronounced maximum near 4.8 eV and conspicuous peaks at around 3.8, 4.2, and 4.6 eV. This indicates that the PL emission discovered in $LaMnO_3$ has the intrinsic origin. Indeed, the pronounced maximum observed in the PL excitation spectra near 4.8 eV corresponds to the resonance energy of the intraband charge-transfer (CT) O($2p$)–Mn($3d$) transition in a nominally stoichiometric $LaMnO_3$ compound [27–29]. In addition, the conspicuous peaks at around 3.8, 4.2, and 4.6 eV correspond to the Mott–Hubbard intersite $d^4d^4 \rightleftharpoons d^5d^3$ transitions between the neighboring Mn^{3+} ions in the $LaMnO_3$ lattice. The excitation energies of the high-spin (HS) and low-spin (LS) $d^4d^4 \rightleftharpoons d^5d^3$ transitions of different symmetry were systematically investigated by using the spectroscopic ellipsometry technique in our earlier studies [15, 16]. According to the results of these studies concerning the e_g–e_g $d^4d^4 \rightleftharpoons d^5d^3$ transitions, (i) the HS state ${}^6A_1$ appears at 2.0 eV, whereas the four LS state transitions appear at higher energies, namely, (ii) ${}^4A_1$ and (iii) ${}^4E_\varepsilon$ at 4.3 eV, (iv) ${}^4E_\theta$ at 4.6 eV, and (v) ${}^4A_2$ at about 6.1 eV. And the peak at 3.8 eV is assigned to the intersite HS t_{2g}–e_g $d^4d^4 \rightleftharpoons d^5d^3$ transition according to our earlier studies [15, 16]. The PL excitation spectra shown in Fig. 5*b* indicate that excitation in the resonant energies of the Mott–Hubbard intersite $d^4d^4 \rightleftharpoons d^5d^3$ transitions leads to the comparatively weak emission. Interestingly, we were not able to detect the PL emission under light excitation above 2.5 eV, in the spectral range covering the pronounced HS-state transition at 2.0 eV (see Fig. 5*b*).

The above consideration implies that under the 4.6 eV light irradiation, the electron–hole pairs resulting from (a) the CT excitation $Mn^{3+} + O^{2-} \rightarrow Mn^{2+} + O^-$ and (b) the Mott–Hubbard excitations $2Mn^{3+} \rightarrow Mn^{2+} + Mn^{4+}$ can be created in $LaMnO_3$. There can be several possibilities for radiative electron–hole recombination. The direct band-to-band recombination gives poor agreement with the position of the PL emission band at 2.5 eV, because common Stokes' shift values are less than 1 eV. Other possibilities could be due to the recombination of generated electron and hole polarons, as well as radiative emission due to the recombination of an exciton. In particular, a charge-transfer vibronic exciton, involving self-trapped electrons and holes bound in pairs, is discussed in relation to the origin of the intrinsic visible band emission peaking at around 2.4 eV (so-called "green luminescence") in $PbTiO_3$, $SrTiO_3$, $BaTiO_3$, $KNbO_3$, and $KTaO_3$ perovskite-type crystals [30]. The "green luminescence" has some similarities with the PL discovered by us in $LaMnO_3$. The relevance of radiative recombination of the charge-transfer vibronic exciton to PL found in $LaMnO_3$ needs to be discussed. In our earlier shell model calculations, we used the Mott–Littleton

approach to evaluate polarization energies in the perovkite $LaMnO_3$ lattice, associated with the hole localized at the O^{2-} anion [27–29]. The full (electronic and ionic) lattice relaxation energy for the hole localized at the O^{2-} site is estimated at 2.38 eV, which is surprisingly large. Because of the large lattice relaxation energy for a hole localized at the O^{2-} site in $LaMnO_3$, the PL emission energy of 2.5 eV is hardly consistent with the recombination energy of the triplet exciton, involving self-trapped charge carriers bound in pairs and localized at the Mn^{3+}–O^{2-}–Mn^{3+} chain. Moreover, due to the Coulomb attraction between the electron and hole polarons in the triplet exciton, the recombination energy should be even lower.

Importantly, in this study we found that spectral features of the discovered PL emission are very similar to those of the dielectric function response $\Delta\varepsilon_2(\nu)$ of the multiplet transitions in the range 2.2–2.9 eV, extracted from the spectroscopic ellipsometry data (see Figs. 3*e,f* and 5*c*). According to our consideration given above, the PL emission in $LaMnO_3$ can be induced more favorably by the intraband CT O(2*p*)–Mn(3*d*) electron excitation and less favorably by the Mott–Hubbard LS intersite $d^4d^4 \rightleftharpoons d^5d^3$ electron excitations. We suggest that nonradiative relaxation of the electronic excitation occurs from these states to the multiplet energy levels in the range 2.2–2.9 eV, discovered from the present spectroscopic ellipsometry study. These states, appearing in the $\varepsilon_2(\nu)$ dielectric function and in the PL emission spectra almost at the same energies, can be assigned to electronic–vibrational (vibronic) excitations of a resonant type.

3. DISCUSSION AND CONCLUSIONS

By using a comprehensive spectroscopic ellipsometry approach, we studied low-energy complex dielectric function spectra, $\varepsilon(\nu) = \varepsilon_1(\nu) + i\varepsilon_2(\nu)$, of the untwinned $LaMnO_3$ single crystal in the temperature range 20–300 K. The low-energy spectra are contributed by a pronounced 2 eV optical band and several narrower higher-energy excitations in the 2.2–2.9 eV spectral range. According to the results of our earlier studies, the 2 eV optical band is associated with the HS state $^6A_1$ transition due to the intersite e_g–e_g electron excitation [15, 16]. However, the nature of the higher-energy excitations in the 2.2–2.9 eV spectral range remained puzzling until now. From the comprehensive temperature measurements of the low-energy complex dielectric function spectra, we discovered that the higher-energy excitations exhibit anomalous temperature dependence around the Néel temperature, $T_N \approx 140$ K. As a result, the higher-energy bands appear as sharp features in the room-temperature (low-temperature) $\varepsilon_2(\nu)$ spectra, or may become almost washed out in the low-temperature (room-temperature) $\varepsilon_2(\nu)$ spectra in the **a**- (**c**-) axis spectra (see Fig. 2*b*). By using classical dispersion analysis, we studied in detail the temperature behavior of the constituent band parameters, namely, of their peak energies, halfwidths, and oscillator strengths (see Fig. 4*d–i*). The disclosed anomalous temperature behavior of the higher-energy bands, in particular, band broadening with decreasing temperature in the **a**-axis spectra (see Fig. 4*f*), excludes their possible origin associated with any kind of defects, or band-to-band transitions, in particular, of the forbidden or weakly allowed *p–d* transitions [18]. We also note that the large characteristic energy scale of the discovered excitations appearing at 2.29 (2.29) eV, 2.41 (2.45) eV, and 2.66 (2.69) eV in the high- (low-) temperature **a**- (**c**-) axis spectra (see Figs. 3*a–f* and 4*d,e*) obviously cannot be compared with the lattice phonon energies.

Here, we also studied photoluminescence emission found for the first time in the $LaMnO_3$ crystal. However, temperature-dependent photoluminescence was earlier found in the doped compound $La_{2/3}Ca_{1/3}MnO_3$ [31]. We now discuss the similarity of their origin. We established that the PL emission is induced most effectively by the intraband charge-transfer O(2*p*)–Mn(3*d*) electronic excitation at 4.6–4.8 eV. The PL emission is observed in a broad spectral range, peaking near 2.5 eV. The analysis, based on our earlier theoretical shell model calculations [27–29], allowed us to exclude possible mechanisms of the discovered PL due to recombination of electron and hole polarons or the charge-transfer vibronic exciton; the latter was discussed in relation to the origin of the intrinsic "green luminescence" in $PbTiO_3$, $SrTiO_3$, $BaTiO_3$, $KNbO_3$, and $KTaO_3$ perovskite-type crystals [30]. Importantly, we found that spectral features of the discovered PL emission are almost coincident with the corresponding contribution $\Delta\varepsilon_2(\nu)$ of the multiple transitions in the range 2.2–2.9 eV, extracted from the dielectric function spectra (see Fig. 5*c*). The evidence of electronic states appearing in the $\varepsilon_2(\nu)$ dielectric function and in the PL emission spectra almost at the same energies can only be explained by supposing resonance-type electronic–vibrational (vibronic) nature of these multiple excitations. Then the charge-transfer O(2*p*)–Mn(3*d*) electronic excitation is followed by nonradiative electronic relaxation to these resonance-type electronic–vibrational (vibronic) energy levels existing

in the range 2.2–2.9 eV. In this case, the mechanism of the PL discovered in $LaMnO_3$ can be associated with radiative recombination from these electronic–vibrational levels to the ground state.

We argue that the discovered excitations are closely related to quantum rotor orbital excitations in a "Mexican hat" potential profile (see Fig. 1*c,d*), which are genuine electronic–vibrational (vibronic) excitations. Their eigenvalues associated with the $\mathbf{A}_1$, $\mathbf{A}_2$, and $\mathbf{E}$ irreducible representations of the C_{3v} symmetry group were earlier estimated by O'Brien [14]. In the dynamic limit (the barrier height $\beta = 0$), energies of the orbital rotor excitations generate a sequence determined by a quadratic dependence on values of the angular momentum j, $\varepsilon = \alpha j^2$. Their energy levels shift up with increasing the barrier height β in the static limit, when the third-order anharmonicity terms result in the appearance of three discrete minima in the trough of the "Mexican hat" (see Fig. 1*d*) [2].

As follows from the diagram, the ground state is represented by the **E** symmetry level with the quantum number of angular momentum around the potential trough $j = \pm 1/2$ (see Fig. 1*d*) [14]. The **E** states are characterized by the angular momentum quantum numbers $j = 1/2, -5/2, 7/2, -11/2, 13/2, \ldots$ and $j = -1/2, 5/2, -7/2, 11/2, -13/2, \ldots$ The value of tunneling splitting α is estimated at about $24\,\mathrm{cm}^{-1}$ from our recent study of anomalous multi-order Raman scattering in $LaMnO_3$ [13]. Using $\alpha = 24\ \mathrm{cm}^{-1}$, we evaluated the following **E** state energies, obeying the quadratic law $\varepsilon = \alpha j^2$, corresponding to the modulus of the angular momentum quantum numbers j given in brackets: 0.7 meV (1/2), 18.6 meV (5/2), 36.4 meV (7/2), 90.0 meV (11/2), 125.7 meV (13/2), 215.0 meV (17/2), 268.5 meV (19/2), 393.5 meV (23/2), 464.9 meV (25/2), 625.6 meV (29/2), 714.9 meV (31/2), 911.2 meV (35/2), 1018.3 meV (37/2), ...

The orbital excitations with low quantum numbers j (1/2, 5/2, 7/2, 11/2, and 13/2) have relatively small energies (up to 0.13 eV) and therefore cannot be distinguished in a wide "background" of the pronounced 2 eV band. We show below that the three narrow higher-energy features discovered in the present comprehensive ellipsometry study at 2.29 (2.29) eV, 2.41 (2.45) eV, and 2.66 (2.69) eV in the high- (low-) temperature **a**- (**c**-) axis spectra (see Fig. 3*a–f*) represent quantum rotor orbital excitations with the higher j values. More exactly, they are actually doublets (which can hardly be resolved in the present optical study) of orbital excitations grouped for the closest j values at (17/2 and 19/2), (23/2 and 25/2), and (29/2 and 31/2), correspondingly. For example, for the **a**-axis data, using the quantum rotor eigenvalues obtained above in the dynamic limit and with the observed peak position shifts from the low-temperature limit (where $\beta \to 0$) to the room-temperature limit (where $\beta \to \infty$) (see Figs. 1*d* and 4*d*) taken into account, we can predict where the associated excitations will arise above the pronounced low-energy optical band located at room temperature at 1.96 eV. Namely, we predict that the orbital rotor excitations for the j values 17/2 and 19/2 will appear as a doublet at (i) $1.96+(0.2150+0.2685)/2+0.08 \approx 2.28$ eV in the **a**-axis room-temperature spectra. Second, we predict that the orbital rotor excitation for the j values 23/2 and 25/2 will appear as a doublet at (ii) $1.96 + (0.3935 + 0.4649)/2 + 0.02 \approx 2.41$ eV in the **a**-axis room-temperature spectra. And finally, we predict that the orbital rotor excitations for the j values 29/2 and 31/2 will appear as a doublet at (iii) $1.96 + (0.6256 + 0.7149)/2 + 0.110 \approx 2.74$ eV in the **a**-axis room-temperature spectra. We also note that the qualitative agreement with the peak energies observed in the **a**-axis spectra at 2.29, 2.41, and 2.66 eV is surprisingly good. Due to the electronic–vibrational (vibronic) nature of the quantum rotor excitations, they appear at the resonant energies in the dielectric function spectra and in the photoluminescence spectra (see Fig. 5*c*).

Visible photoluminescence of the doped compound $La_{2/3}Ca_{1/3}MnO_3$ in the temperature range 138–293 K was found in [31]. It was established that the photoluminescence band is represented by the main broad band centered at 1.75 eV, with the shoulders at 1.52 and 1.92 eV. On the other hand, in optical spectra of the doped compounds, in particular, $Nd_{0.7}Sr_{0.3}MnO_3$, the low-energy absorption band is centered around 1.2 eV at room temperature [32]. We suggest that the observed photoluminescence peaks can be associated with the quantum rotor energy excitations (i)–(iii), appearing as higher-energy satellites of the 1.2 eV optical band at the respective estimated energies of 1.52, 1.65, and 1.98 eV.

We conclude from our study that the orbital rotor excitations for the higher j values ($j \gtrsim 35/2$) seemingly cannot be observed, because they are superimposed with the intense and relatively wide band at around 2.8 eV. We would also guess that the quantum rotor orbital excitations cannot have energies above the JT splitting energy Δ_{JT} and must disappear at higher energies. Here, we suggest that the relatively wide 2.8 eV component is associated with electronic transitions between the double-valued "Mexican hat" energy surfaces, of $4\Delta_{JT}$ at the minimum. This is in agreement with our earlier estimates of the JT energy in $LaMnO_3$, $\Delta_{JT} \approx 0.7$ eV [16].

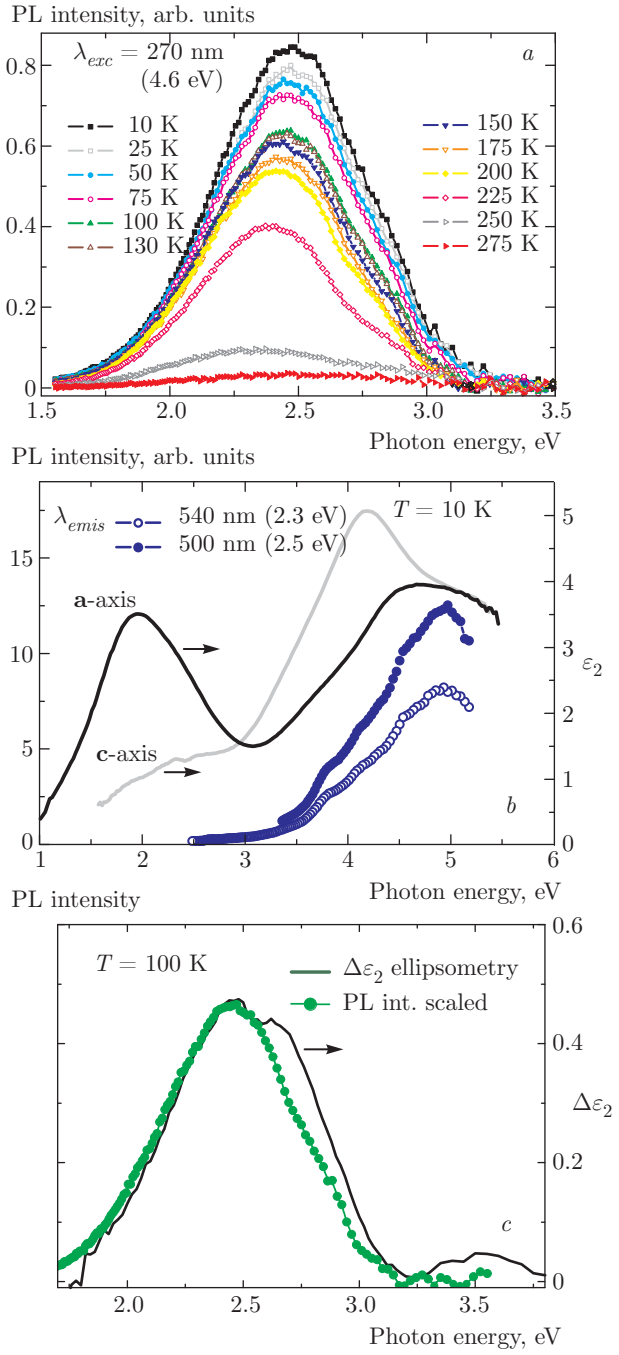

Fig. 5. (Color online) (a) The photoluminescence (PL) emission spectra measured on the same $LaMnO_3$ crystal at different temperatures from 10 to 300 K under 4.6 eV light excitation. (b) The associated PL excitation spectra registered for the fixed PL emission energies of 2.3 and 2.5 eV at $T \approx 10$ K (shown by the respective open and filled symbols). The PL excitation spectra are superimposed with the **a**- and **c**-axis dielectric function spectra $\varepsilon_2^{\mathbf{a},\mathbf{c}}(\nu)$ of the untwinned $LaMnO_3$ single crystal, corresponding to those shown in Fig. 2b. (c) The extracted cumulative contribution of the higher-energy transitions in the range 2.2–2.9 eV to the ε_2 dielectric function in the **c**-axis, resulting from the dispersion analysis (see Fig. 3c), compared with the scaled PL intensity ($T = 100$ K)

Moreover, we found that the band halfwidth increases strongly for the lower-lying 2.29 eV band, but weaker for the higher-lying 2.41 eV band, as the temperature decreases below $T_N \approx 140$ K (see Fig. 4f). The disclosed temperature behavior of the **a**-axis bands is certainly beyond the lattice anharmonicity principle, which suggests band narrowing with lowering the temperature. We suggest that this behavior can be associated with dissipation of the quantum rotor excitations as their energy is lowered with decreasing the anharnomicity barrier height β, approaching the barrier top. The disclosed temperature behavior of the **c**-axis bands suggests opposite trends.

Finally, we discuss the observed temperature behavior of the oscillator strength of the low-energy bands (shown in Figs. 4c,h,i). According to the results of our earlier studies, the 2 eV optical band is associated with the HS-state $^6A_1$ transition due to the intersite e_g–e_g electron excitation [15, 16]. In the framework of the superexchange model, the **a**- and **c**-components of the oscillator strength of the 2 eV band shift in an opposite way near T_N, being influenced by antiferromagnetic spin–spin correlations between the Mn^{3+} spins (see Fig. 4c). Since the quantum rotor excitations appear as narrow sidebands accompanying the electron transition between the JT split orbitals on neighboring Mn^{3+} ions at 2 eV, the same trend holds for their oscillator strength (in Fig. 4h,i).

In addition, we would like to point out some important consequences following from our present study. In the high-temperature static limit, depopulation of the quantum rotor energy states as the temperature decreases can result in structural instabilities in orthorhombic manganites at temperatures far below the orbital temperature, T_{oo}. Recently, ESR evidence for partial melting of the orbital order in $LaMnO_3$ below $T_{oo} = 780$ K at $T^* = 550$ K was obtained [33]. Indeed, depopulation of the electron–vibrational quantum rotor energy level with the angular momentum quantum number $j = 7/2$, whose energy is shifted from the dynamic to static limit by about 10 meV (that is, to about 46 meV), can result in orbital structure instabilities below about 550 K. However, one can expect spectacular phenomena in the low-temperature dynamic limit of orthorhombic manganites, when depopulation of the quantum rotor energy levels near the ground state (in particular, for $j = 5/2$ with the eigenvalue 18.6 meV $\approx$ 220 K) can result in low-temperature phase transitions, also facilitating the formation of the long-range magnetic order or ferroelectric phase in orthorhombic manganites. These changes can be accompanied by softening of the Raman-active phonon

modes, in agreement with the available observations [13, 34, 35]. Similar behavior was noticed in another classic example of orbital compound, $KCuF_3$. There, the anomalous softening and splitting of the Raman-active modes near T_N is related to the existence of nearly degenerate spin and orbital configurations and an unidentified structural transition [36].

In summary, in order to increase our understanding of the mechanism of the low-temperature phase transitions associated with temperature populations of the quantum rotor energy states, the nature of the Jahn–Teller ground state in orthorhombic manganites and other systems of magnetic compounds with JT ions (such as Mn^{3+} and Cu^{2+}) needs to be studied in more detail.

We thank A. Balbashov for growing the crystals. The authors acknowledge the fruitful discussions with D. Khomskii, M. Skorikov, V. Vinogradov, and N. Sibeldin. We also thank A. Kulakov for detwinning the crystal, J. Strempfer, I. Zegkinoglou, and M. Schulz for characterization of the $LaMnO_3$ sample, and V. Bogatirenko for participation in the photoluminescence measurements. This work was supported by RFBR (grants №№ 14-02-00276, 16-02-00304).

REFERENCES

1. H. A. Jahn and E. Teller, Proc. R. Soc. London A **161**, 220 (1937).

2. U. Öpik and M. H. L. Pryce, Proc. Roy. Soc. A **238**, 425 (1957).

3. A. M. Stoneham, *Theory of Defects in Solids*, Clarendon Press, Oxford (1975).

4. M. D. Kaplan and B. G. Vekhter, *Cooperative Phenomena in Jahn–Teller Crystals*, Plenum, New York (1995).

5. I. B. Bersuker, *Jahn–Teller Effect*, Cambridge University Press, New York, Melbourne, Cape Town, Singapore, Sao Paulo (2006).

6. I. B. Bersuker, B. G. Vekhter, and I. I. Ogurtsov, Sov. Phys. Uspekhi **18**, 569 (1975) [Usp. Fiz. Nauk **116**, 605 (1975)].

7. J. B. Goodenough, *Magnetism and the Chemical Bond*, Wiley Interscience, New York (1963).

8. K. I. Kugel and D. I. Khomskii, JETP **37**, 725 (1973).

9. Y. Tokura and N. Nagaosa, Science **288**, 462 (2000).

10. E. Pavarini and E. Koch, Phys. Rev. Lett. **104**, 086402 (2010).

11. J. Rodríguez-Carvajal, M. Hennion, F. Moussa et al., Phys. Rev. B **57**, R3189 (1998).

12. M. W. Kim, S. J. Moon, J. H. Jung et al., Phys. Rev. Lett. **96**, 247205 (2006).

13. N. N. Kovaleva, O. E. Kusmartseva, K. I. Kugel et al., J. Phys.: Condens. Matter **25**, 155602 (2013).

14. M. C. M. O'Brien, Proc. Roy. Soc. A **281**, 323 (1964).

15. N. N. Kovaleva, A. V. Boris, C. Bernhard et al., Phys. Rev. Lett. **93**, 147204 (2004).

16. N. N. Kovaleva, A. M. Oleś, A. M. Balbashov et al., Phys. Rev. B **81**, 235130 (2010).

17. K. Tobe, T. Kimura, Y. Okimoto, and Y. Tokura, Phys. Rev. B **64**, 184421 (2001).

18. A. S. Moskvin, A. A. Makhnev, L. V. Nomerovannaya, N. N. Loshkareva, and A. M. Balbashov, Phys. Rev. B **82**, 035106 (2010).

19. A. M. Balbashov, S. G. Karabashev, Y. M. Mukovsky, and S. A. Zverkov, J. Cryst. Growth **167**, 365 (1996).

20. A. M. Balbashov and S. K. Egorov, J. Cryst. Growth **52**, 498 (1981).

21. K. Hirota, N. Kaneko, A. Nishizawa, and Y. Endoh, J. Phys. Soc. Jpn. **65**, 3736 (1996).

22. J. Kircher, J. Humlicek, M. Garriga et al., Physica C **192**, 473 (1992).

23. J. W. Allen and J. C. Mikkelsen, Phys. Rev. B **15**, 2952 (1977).

24. W. Hayes and A. M. Stoneham, *Defects and Defect Processes in Nonmetallic Solids*, John Wiley Sons, New York, Chichester, Brisbane, Toronto, Singapore (1985).

25. I. S. Smirnova, A. V. Bazhenov, T. N. Fursova et al., Physica B **403**, 3896 (2008).

26. N. N. Kovaleva, A. V. Boris, L. Capogna et al., Phys. Rev. B **79**, 045114 (2009).

27. N. N. Kovaleva, J. L. Gavartin, A. L. Shluger, A. V. Boris, and A. M. Stoneham, JETP **121**, 210 (2002) [Zh. Eksp. Teor. Fiz. **94**, 178 (2002)].

28. N. N. Kovaleva, J. L. Gavartin, A. L. Shluger, A. V. Boris, and A. M. Stoneham, Physica B **312–313**, 734 (2002).

29. N. N. Kovaleva, J. L. Gavartin, A. V. Boris, and A. M. Stoneham, Physica B **312–313**, 737 (2002).

30. R. I. Eglitis, V. A. Trepakov, S. E. Kapphan, and G. Borstel, Sol. St. Comm. **126**, 301 (2003).

31. T. Ding, W. T. Zheng, H. W. Tian et al., Sol. St. Comm. **132**, 815 (2004).

32. S. Kaplan, M. Quijada, H. D. Drew et al., Phys. Rev. Lett. **77**, 2081 (1996).

33. S. Schaile, H.-A. Krug von Nidda, J. Deisenhofer, M. V. Eremin, Y. Tokura, and A. Loidl, Phys. Rev. B **90**, 054424 (2014).

34. E. Granado, N. O. Moreno, A. García et al., Phys. Rev. B **58**, 11435 (1998).

35. J. Laverdiére, S. Jandl, A. A. Mukhin et al., Phys. Rev. B **73**, 214301 (2006).

36. J. C. T. Lee, S. Yuan, S. Lal et al., Nature Phys. **8**, 63 (2012).